INDIAN JOURNAL OF SCIENCE AND TECHNOLOGY

ORIGINAL ARTICLE

Haar Wavelet Operational Matrix Method for the Solution of Magnetohydrodynamic Lubrication Problem of Porous Rough Plates for Squeeze Films

S C Shiralashetti[1]*, N T Vatsala[1]

1 Department of Mathematics, Karnatak University, Dharwad-580003, Karnataka, India

OPEN ACCESS

Received: 19/10/2025

Accepted: 07/01/2026

Published: 24/01/2026

Citation: Shiralashetti SC, Vatsala NT (2026) Haar Wavelet Operational Matrix Method for the Solution of Magnetohydrodynamic Lubrication Problem of Porous Rough Plates for Squeeze Films. Indian Journal of Science and Technology 19(3): 116-132. https://doi.org/10.17485/IJST/v19i3.1717

* **Corresponding author**.

scshiralashetti@kud.ac.in, shiralashettisc@gmail.com

Funding: None

Competing Interests: None

Published By Indian Society for Education and Environment (iSee)

ISSN
Print: 0974-6846
Electronic: 0974-5645

Abstract

Objectives: In this study, a rough upper plate and a porous lower plate, which are lubricated with an electrically conducting couple-stress fluid in a magnetic field, are examined under magnetohydrodynamic squeeze-film lubrication. The goal is to create a precise and effective Haar wavelet-based computational framework. This framework will capture the combined effects of non-Newtonian properties, porosity, surface roughness, and magnetic influences on lubrication performance. **Methods:** The Haar Wavelet Operational Matrix of Integration (HWOMM) helps derive the modified MHD Reynolds equation, considering longitudinal roughness. This method offers strong numerical stability and fast convergence. It does this by turning the governing nonlinear partial differential equation into a compact nonlinear algebraic system. **Findings:** According to the numerical results, surface imperfections improve load support. Magnetic intensity increases hydrodynamic pressure, load-carrying capacity, and squeeze-film durability. Fluid infiltration into the substrate leads to increased permeability of the porous layer, which reduces pressure development. Couple tensions extend the lubrication period by delaying film thinning. The Haar wavelet formulation provides smoother solution profiles, better accuracy, and requires less processing effort than finite-difference methods. **Novelty:** The Haar Wavelet Operational Matrix of Integration for MHD squeeze-film lubrication with stochastic roughness, porous media, magnetic fields, and couple-stress fluid dynamics is used for the first time in this work. This new approach addresses tightly linked electromagnetic, rheological, and surface effects within a single wavelet framework. This is different from earlier wavelet-based lubrication studies, which focused on smooth geometries, Newtonian fluids, or non-magnetic conditions. The method's strong numerical stability and efficiency allow for the identification of lubrication features that traditional solution methods cannot capture.

Keywords: Magnetohydrodynamic lubrication (MHD); Porous rough plates; Squeeze film; Hartmann number; Haar wavelet Operational matrix method (HWOMM)

1 Introduction

Magnetohydrodynamic (MHD) squeeze-film lubrication has received a lot of attention recently because it is important for engineering systems. Here, controlling electrically conducting fluids in magnetic fields is crucial. The interaction of electromagnetic forces, surface texture, and fluid microstructure affects film pressure, load-carrying capacity, and dynamic stability. These are vital factors in designing modern bearings and actuators [(1)].

Early studies on MHD lubrication in thrust bearings under external pressure were reported in [(2)]. This work set the stage for more research on various bearing types, including finite journal bearings [(3)], poroelastic bearings [(4)], and narrow journal bearings [(5)]. Christensen's stochastic model [(4)] provided a way to analyse surface roughness, pinpointing longitudinal and transverse roughness patterns that significantly impact pressure and film properties. Later studies expanded these models to squeeze-film systems with porous plates [(6,7)]. They showed that porosity can improve load-carrying capacity and damping effects, while roughness may either enhance or hinder lubrication performance, depending on geometry and flow conditions [(6,8,9)].

Incorporating MHD effects into squeeze-film lubrication has been particularly useful for systems that use electrically conducting couple-stress fluids. This is common in aerospace, biomedical, and microelectromechanical devices. The addition of a magnetic field changes fluid flow dynamics, adds damping, and stabilises thin films under extreme conditions [(4)]. However, the modified MHD Reynolds equation, which combines the effects of magnetism, surface roughness, and porosity, is highly nonlinear [(10–12)]. This creates coupled partial differential equations (PDEs) that are hard to solve accurately with traditional numerical methods.

Traditional methods like the Finite Difference Method (FDM) and Finite Element Method (FEM) offer workable approximations but have significant drawbacks, are high computational cost because they need dense grids, slow convergence in nonlinear or multiscale problems and reduced accuracy when dealing with sharp gradients or complex boundary conditions.

To overcome these limitations, wavelet-based numerical methods have become effective alternatives. Wavelets can capture local changes, handle discontinuities, and lower computational effort through compact support and multiresolution capabilities. One method, the Haar Wavelet Operational Matrix Method (HWOMM), is particularly attractive due to its simplicity, orthogonality, and computational efficiency [(13–16)]. It converts differential equations into algebraic systems, allowing for quick and stable convergence while keeping high precision. Previous studies [(17–24)] have successfully used wavelet-based techniques for fluid flow, diffusion, and nanofluid problems, but their use in MHD squeeze-film lubrication between rough porous plates has not been explored.

Although there are many studies on MHD lubrication, most look at individual factors like magnetic field, surface roughness, or porosity. Few have tried to model how these factors work together, even though they significantly affect the performance of modern lubrication systems. Additionally, traditional numerical methods, such as FDM and FEM, do not provide the accuracy and speed needed to solve the nonlinear coupled Reynolds equation effectively. No previous research has used the Haar Wavelet Operational Matrix of Integration (HWOMM) for these lubrication issues [(20,21)], where complex boundary interactions and multiscale effects are important.

To tackle these problems, this work uses HWOMM to solve the modified MHD Reynolds equation for squeeze-film lubrication between a rough upper plate and a porous lower plate [(7)]. This method reduces computational complexity, eliminates discretisation errors, and produces highly accurate solutions for pressure and load capacity. The main contributions and innovations of this study are: The first application of the Haar Wavelet Operational Matrix of Integration Method (HWOMM) to MHD squeeze-film lubrication with rough and porous surfaces. A unified framework that captures the simultaneous effects of the magnetic field, surface roughness, porosity, and couple-stress. These factors have been treated separately in previous studies. Superior numerical performance, achieving about a 70% reduction in computation time and less than 0.3% error compared to finite-difference results. Quantitative insight into how physical parameters affect pressure, load capacity, and squeeze-film duration. This provides a better understanding of MHD-based lubrication dynamics.

2 Mathematical Formulation

The bottom plate is made of a permeable material, while the top plate has a textured surface and is subjected to a uniform external magnetic field (M). The film thickness $\hbar$ consists of a nominal smooth section and an additional component due to surface roughness. The top plate moves toward the lower plate with a constant velocity $\frac{d\hbar}{dt}$. In a schematic representation of Figure 1, a squeeze-film lubricant is seen between two rectangular plates. The rough upper plate approaches the lower porous plate at a velocity $-\frac{\partial \hbar}{\partial t}$, and the fluid in the film is assumed to be an incompressible, electrically conducting couple-stress fluid with constant (isothermal) viscosity. Within the framework of lubrication theory, fluid inertia is neglected, except for the Lorentz force contribution, while body forces are assumed to be negligible. The magnetohydrodynamic equations of motion,

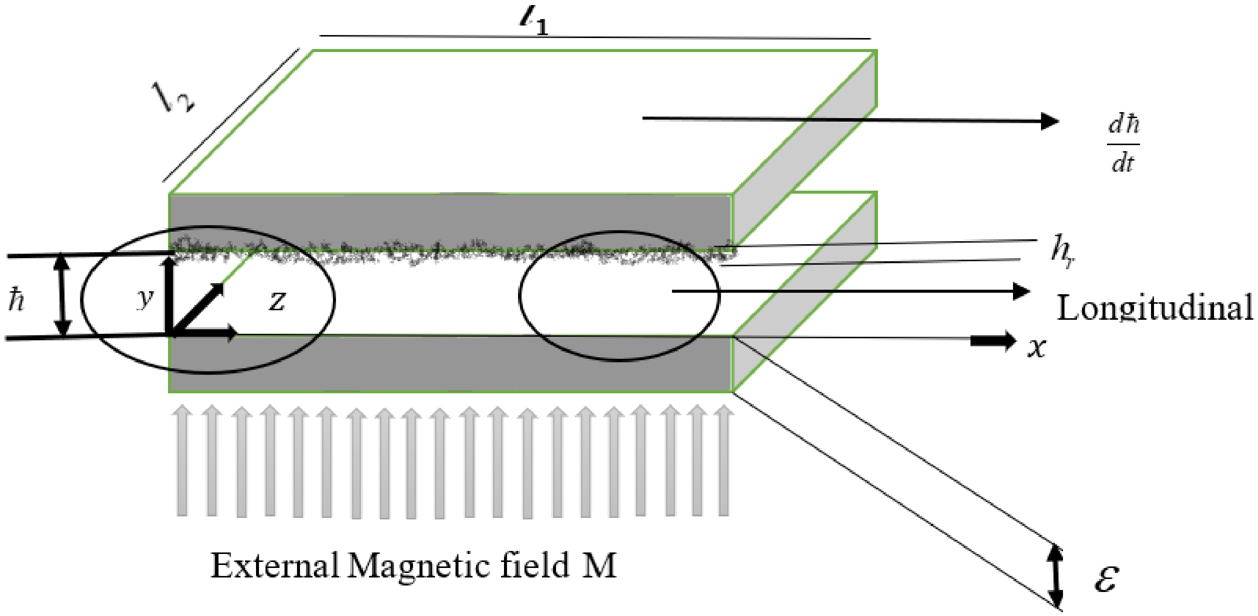

Fig 1. Schematic of MHD squeeze-film lubrication between two finite rectangular plates. It shows the squeeze motion, longitudinal roughness, porous substrate, and magnetic field. The pressure at the plate edges is assumed to be ambient.

shown in rectangular coordinates, give the result of the hydrodynamic lubrication theory that applies to thin films under these presumptions.

$$\frac{\partial P}{\partial x} = \eta \frac{\partial^2 v_x}{\partial y^2} - \mu \frac{\partial^4 v_x}{\partial y^4} - \kappa H^2 v_x, \tag{1}$$

$$\frac{\partial P}{\partial y} = 0, \tag{2}$$

$$\frac{\partial P}{\partial z} = \eta \frac{\partial^2 v_z}{\partial y^2} - \mu \frac{\partial^4 v_z}{\partial y^4} - \kappa H^2 v_z, \tag{3}$$

$$\frac{\partial v_x}{\partial x} + \frac{\partial v_y}{\partial y} + \frac{\partial v_z}{\partial z} = 0. \tag{4}$$

Where P represents the pressure which exist distributions in the fluid area, and fluid viscosity is denoted by η, κ is the voltage of the electrical potential,v_x, v_y and v_z are the fluid velocities in the $x, yandz$ direction correspondingly. The magnetic field also known as M that is lubricant's conductance. Polar additives are incorporated into nonpolar lubricants caused to the addition of μ in Eqs. (1) and (3) above. The squared length dimension, which describes the couple-stress fluid is possessed by a quantity $\frac{\mu}{\eta}$.

For the velocity factors, the necessary boundary conditions are:
at $y = 0 : v_x = 0, v_z = 0, v_y = {v_y}^*$,

$$\frac{\partial^2 v_x}{\partial y^2} = 0, \frac{\partial^2 v_z}{\partial y^2} = 0, \tag{5}$$

at $y = \hbar : v_x = 0, v_y = -\frac{\partial \hbar}{\partial t}$,

$$v_z = 0, \frac{\partial^2 v_x}{\partial y^2} = 0, \frac{\partial^2 v_z}{\partial y^2} = 0, \tag{6}$$

Where $\frac{\partial \hbar}{\partial t}$ Denotes the approach velocity of the upper plate relative to the lower plate. The last two conditions in Eqs. (5) and (6) state that couple-stress effects vanish at the bearing boundaries. The film thickness $\hbar$ consists of two components that separate the narrow gap.

$$\hbar = h_0(t) + h_r(x, z, \xi), \tag{7}$$

where $h_0(t)$ is the fluid film region's standard smooth portion height and index parameter ξ, which defines a certain structure of roughness, and $h_r(x, z, \xi)$ is the portion attributed to the surface irregularities measured relative to the nominal level and follows a random pattern variable amount with zero average. The Stokes equation may be used to obtain the modified form of Darcy's law, which controls the flow of a couple-stress fluid in a porous medium with a magnetic field applied to it. Then, by using statistical averages and simplifications, we have the following formulation.

$$v_x{}^* = \frac{K}{\eta(1 + \varphi M^2 - \beta)} \frac{\partial p_i{}^*}{\partial x}, \tag{8}$$

$$v_y{}^* = -\frac{K}{\eta(1 - \beta)} \frac{\partial p_i{}^*}{\partial y}, \tag{9}$$

$$v_z{}^* = -\frac{K}{\eta(1 - \varphi M^2 - \beta)} \frac{\partial p_i{}^*}{\partial z}, \tag{10}$$

$$\nabla Q^* = 0, \tag{11}$$

where $Q^* = (v_x{}^*, v_y{}^*, v_z{}^*)$, $\beta = (\mu/\eta)/K$, and $M = \sqrt{\kappa/\eta} H h_*$, K represents the permeability of the porous material, $\varphi = K/h_*{}^2$ is the proportion of void volume in the porous material to its overall volume, which is known as the normalised porosity factor, $M = \sqrt{\kappa/\eta} H h_*$ a dimensionless number called the Hartmann number indicates how significant electromagnetic forces are in a fluid flow in relation to viscous forces, and the minimum thickness is h_*. The lubricant's polar additives limit the Darcy flow across the porous medium by blocking the voids in the porous layer if $\beta = O$. In contrast, the polar additives may readily percolate into the porous media with smaller values of β since their size is less than the pore size. Eqs. (8), (9), and (10). These equations reduce to the case of Newtonian flow, where $\mu = 0 = \beta = M$, in the absence of magnetic effects. From Eqs. (8), (9), (10), and (11), it is easily evident that pressure $p_i{}^*$.

The pressure in the porous zone satisfies Laplace's equation.

$$\frac{\partial^2 p_i{}^*}{\partial x^2} + d \frac{\partial^2 p_i{}^*}{\partial y^2} + \frac{\partial^2 p_i{}^*}{\partial z^2} = 0, \tag{12}$$

Where $d = (1 + \varphi M^2 - \beta)/(1 - \beta)$. Integrating Eq. (12) concerning y throughout the porous thickness layer ε, making use of the strong backing limit conditions $\frac{\partial p_i{}^*}{\partial y} = 0$ at $z = -\varepsilon$.

$$\text{we get,} \qquad \left.\frac{\partial p_i{}^*}{\partial y}\right|_{y=0} = -\frac{1}{d} \int_{-\varepsilon}^{0} \left(\frac{\partial^2 p_i{}^*}{\partial x^2} + \frac{\partial^2 p_i{}^*}{\partial z^2} \right) dy, \tag{13}$$

The thickness of the porous layer ε [7]. The estimate suggests that the porous layer thickness is less than that of the fluid film. Using the condition of pressure continuity $p_i{}^* = P$ at the porous contact $y = 0$, the equation Eq. (13) becomes:

$$\left.\frac{\partial p_i{}^*}{\partial y}\right|_{y=0} = -\frac{\varepsilon}{d} \left(\frac{\partial^2 p_i{}^*}{\partial x^2} + \frac{\partial^2 p_i{}^*}{\partial z^2} \right) \tag{14}$$

To address the issue, the momentum equations (1)-(3), the continuity equation (4), and, in connection with Eq. (14), it is necessary to apply the boundary conditions Eqs. (5) and (6).

3 Methodology

Closed-form velocity profiles in the v_x and v_z directions, expressed in terms of pressure gradients, are derived by applying the no-slip and vanishing couple-stress boundary conditions (5) and (6). Then, we integrate the momentum equations (1) and (3) twice with respect to the transverse coordinate y. We obtain a Reynolds-type equation by inserting these velocity expressions into the continuity equation (4) and integrating over the thickness of the lubricant film. The function $D(\hbar, k_1, k_2)$ describes how the magnetic field and couple-stress rheology together affect the volumetric flow rate. This relationship logically follows from the integration.

$$\frac{\partial}{\partial x}\left\{D(\hbar, k_1, k_2)\frac{\partial P}{\partial x}\right\} + \frac{\partial}{\partial z}\left\{D(\hbar, k_1, k_2)\frac{\partial P}{\partial z}\right\} = \frac{\eta M^2({k_1}^2 - {k_2}^2)}{{h_*}^2}\frac{\partial H}{\partial t} + 12K\left.\frac{\partial {p_i}^*}{\partial y}\right|_{y=0}, \tag{15}$$

Where $D(\hbar, k_1, k_2) = \hbar\left({k_1}^2 - {k_2}^2\right) - \frac{2{k_1}^2}{k_2}\tan h\left(\frac{k_2\hbar}{2}\right) + \frac{2{k_2}^2}{k_1}\tan h\left(\frac{k_1\hbar}{2}\right)$

$$k_1 = \frac{\tau}{\sqrt{2}h_*}\left(1 + \sqrt{1 - \frac{4M^2}{{h_*}^2\tau^2}}\right)^{1/2} \text{ and } k_2 = \frac{\tau}{\sqrt{2}h_*}\left(1 - \sqrt{1 - \frac{4M^2}{{h_*}^2\tau^2}}\right)^{1/2}, \text{ where } \tau = \sqrt{\frac{\eta}{\mu}}, \tag{16}$$

h_* Represents the minimal thickness. The parameter couple-stress (τ) was introduced in charge of the non-Newtonian impact of couple-stress fluid, then they are projected to have a greater impact on lower values of τ, whereas larger values have less impact. Implementing Eq. (14) into Eq. (15) and reordering the terms, we get,

$$\frac{\partial}{\partial x}\left\{\left[D(\hbar, k_1, k_2) + \frac{12K\varepsilon}{d}\right]\frac{\partial P}{\partial x}\right\} + \frac{\partial}{\partial z}\left\{\left[D(\hbar, k_1, k_2) + \frac{12K\varepsilon}{d}\right]\frac{\partial P}{\partial z}\right\} = \frac{\eta M^2({k_1}^2 - {k_2}^2)}{{h_*}^2}\frac{\partial H}{\partial t} \tag{17}$$

Fluid exchange between the lubricant coating and the porous substrate is considered in the last term of Equation (15). The normal pressure gradient in the porous medium is defined by the second derivatives of the film pressure. This uses the thin porous-layer approximation and assumes pressure continuity at the fluid–porous interface. When this relation is inserted into Eq. (15), the permeability-dependent term $\frac{12K\varepsilon}{d}$ changes the Reynolds operator additively, leading to Eq. (17). With this formulation, a single modified Reynolds equation can control the pressure field in both the film and porous areas.

The film thickness has two parts: a nominal component and a random fluctuation caused by surface roughness. Next, we assume that longitudinal roughness is statistically stationary. We apply Christensen's stochastic averaging theory to Eq. (17). Instead of dealing with individual asperities, the expectation operator works on the flow coefficients with the local film thickness. This creates averaged Reynolds operators that capture the effects of roughness.

$$\frac{\partial}{\partial x}\left\{E_e\left(\left[D(\hbar, k_1, k_2) + \frac{12K\varepsilon}{d}\right]\right)\frac{\partial P}{\partial x}\right\} + \frac{\partial}{\partial z}\left\{E_e\left(\left[D(\hbar, k_1, k_2) + \frac{12K\varepsilon}{d}\right]\right)\frac{\partial P}{\partial z}\right\} = \frac{\eta M^2({k_1}^2 - {k_2}^2)}{{h_*}^2}\frac{\partial E_e[H]}{\partial t} \tag{18}$$

The expectation operator

$$E_e(\cdot) \text{ is } E_e(\cdot) = \int_{-\infty}^{\infty}(\cdot) f(h_r)dh_r, \tag{19}$$

$f(h_r)$ Represents the probability distribution function for random events. Variable: Roughness striations on bearing surfaces are typically modelled using a polynomial function that approximates a Gaussian distribution.

$$f(h_r) = \begin{cases} \frac{35}{32c^7}(c^2 - {h_r}^2)^3, -c \le h_r \le c \\ 0, otherwise \end{cases} \tag{20}$$

$c = \pm\sigma$, where σ is the standard deviation. Christensen's averaging rules allow us to separate the expectation operator from the pressure gradients for one-dimensional longitudinal roughness. This leads to anisotropic roughness effects being shown in the averaged Reynolds equation. The equation reveals different effective flow coefficients in the longitudinal and transverse directions. We obtain the simplified averaged Reynolds equation in Eq. (21) by applying these relations to Eq. (18).

$$E_e\left(D(\hbar, k_1, k_2)\frac{\partial P}{\partial x}\right) = E_e\left(D(\hbar, k_1, k_2)\frac{\partial E_e(P)}{\partial x}\right), E_e\left(D(\hbar, k_1, k_2)\frac{\partial P}{\partial z}\right) = E_e\left(D(\hbar, k_1, k_2)\frac{\partial E_e(P)}{\partial z}\right),$$

$$\frac{\partial}{\partial x}\left\{E_e\left(\left[D(\hbar,k_1,k_2)+\frac{12K\varepsilon}{d}\right]\right)\frac{\partial E_e(P)}{\partial x}\right\}+\frac{\partial}{\partial z}\left\{E_e\left(\left[D(\hbar,k_1,k_2)+\frac{12K\varepsilon}{d}\right]\right)\frac{\partial E_e(P)}{\partial z}\right\}=\frac{\eta M^2({k_1}^2-{k_2}^2)}{{h_*}^2}\frac{\partial h_0}{\partial t} \quad (21)$$

To resolve the modified Reynolds equation, we utilise the specified boundary conditions.

$$\begin{aligned} E_e(P(0,z)) &= E_e(P(l_1,z))=0, \\ E_e(P(x,0)) &= E_e(P(x,l_2))=0, \end{aligned}$$

Surface dimensions along x and z directions are denoted by l_1 and l_2, respectively. The pressure distribution remains constant beyond the film zone. Inviting the appropriate variables and nondimensional parameters.

$$\overline{x}=\frac{x}{l_1},\overline{z}=\frac{z}{l_2},\overline{\hbar}=\frac{\hbar}{h_*},\text{ and }\overline{\tau}=\tau h_*,\psi=\frac{K\varepsilon}{{h_*}^3},C=\frac{c}{h_*},P=-\frac{{h_*}^3E(P)}{l_1\mu\partial\hbar/\partial t},ƛ=\frac{l_2}{l_1}, \quad (23)$$

In this case, $\overline{\hbar}$ indicates the nondimensional film thickness. ƛ is the bearing's geometric aspect ratio. η is used only for the couple-stress viscosity.

Lastly, the governing equation is scaled based on characteristic film thickness, bearing dimensions, and squeezing velocity by including the nondimensional variables and parameters specified in Eq. (23). The nondimensional modified Reynolds equation (24), which serves as the governing equation for the following Haar wavelet-based numerical solution, is derived by substituting into Eq. (21). we derive the nondimensional Reynolds equation under the conditions of Eq. (22).

$$\frac{\partial}{\partial x}\left\{E_e\left(\left[D(\hbar,k_1,k_2)+\frac{12\psi}{d}\right]\right)\frac{\partial P}{\partial x}\right\}+\frac{1}{ƛ}\frac{\partial}{\partial z}\left\{\left(\frac{1}{E_e\left(D(\hbar,k_1,k_2)\right)}+\frac{12\psi}{d}\right)\right\}\frac{\partial P}{\partial z}=-M^2({k_1}^2-{k_2}^2) \quad (24)$$

$$\text{Where, } E_e\left(D(\hbar,k_1,k_2)\right)=\frac{35}{32C^7}\int_{-C}^{C}D(\hbar,k_1,k_2)\,(C^2-{h_r}^2)^3dh_r, \quad (25)$$

$$E_e\left(\frac{1}{D(\hbar,k_1,k_2)}\right)=\frac{35}{32C^7}\int_{-C}^{C}\frac{1}{D(\hbar,k_1,k_2)}(C^2-{h_r}^2)^3dh_r,$$

$$k_1=\frac{\tau}{\sqrt{2}}\left(1+\sqrt{1-\frac{4M^2}{\tau^2}}\right)^{1/2},k_2=\frac{\tau}{\sqrt{2}}\left(1-\sqrt{1-\frac{4M^2}{\tau^2}}\right)^{1/2}, \quad (26)$$

The pressure boundary conditions for the finite rectangular bearing geometry shown in Fig. 1 are as follows.

Also, the conditions given at their boundary are:

$$P(0,z)=P(1,z)=0,P(x,0)=P(x,1)=0, \quad (27)$$

For squeeze-film lubrication problems involving finite plates, these criteria show the ambient pressure at the bearing edges. The modified Reynolds equation implicitly includes the kinematic boundary conditions tied to the squeeze motion of the upper plate, no-slip conditions at the solid surfaces, vanishing couple stresses, and fluid exchange at the porous interface that were already accounted for in the velocity formulation. As a result, only the pressure boundary conditions needed to solve the Reynolds problem are stated in Eq. (27).

Equation (27) sets the ambient pressure at the bearing edges, which relates to an open finite squeeze film. All velocity-related boundary conditions are included in the governing Reynolds equation.

The aspect ratio ƛ, the nondimensional permeability parameter ψ and the nondimensional roughness parameter C. Considering all parameters, Pressure variation in the fluid portion is simulated, and the transformed Reynolds equation (Eq. 24) is used for a longitudinal roughness pattern with specified boundary conditions. Eq. (27) is solved. The solution approach involves numerical solutions for the Reynolds equation and associated integral formulations in Eqs. (25) and (26). For $\psi=0$ and $\tau\to\infty$ The present formulation reduces to the results of Bujurke and Kudenatti[9] for Newtonian, non-porous materials.

Algorithm to solve Non dimensional Reynolds equation using HWOMM

The Haar Wavelet Operational Matrix Method is used to solve the nondimensional modified Reynolds equation (Eq. 24) as follows:

Step 1: The unknown pressure function $P(x,z)$ is approximated by a finite Haar wavelet series that uses 2^J basis functions in each spatial direction.

Step 2: Haar operational matrices of integration are created to change spatial derivatives in the governing equation into algebraic matrix forms.

Step 3: The modified Reynolds equation is evaluated at chosen Haar grid points or collocation points, and the expected terms in Eqs. (25) – (26) are computed numerically.

Step 4: The pressure boundary conditions (Eq. 27) are applied directly to the algebraic system by adjusting the corresponding rows of the coefficient matrix.

Step 5: The resulting discretized equation produces a nonlinear algebraic system in terms of the Haar coefficients.

Step 6: This system is solved step by step until it converges, after which the pressure distribution is reconstructed from the Haar expansion.

Step 7: Bearing performance characteristics are found by integrating the computed pressure field numerically.

General 2-D Partial differential equations steps are explained in Section 4.

4 Mathematical Preliminaries of Haar Wavelet and Operational Matrix Method

The Haar wavelet family consists of a scaling function and a mother wavelet, both defined on the interval $[0,1]$ [17].

$$H_1(t) = \begin{cases} 1, fort \in [0,1) \\ 0 elsewhere, \end{cases} \quad \text{(Generating function)} \tag{28}$$

$$H_2(t) = \begin{cases} 1, fort \in [0,1/2) \\ -1, fort \in [1/2,1) \\ 0, elsewhere, \end{cases} \quad \text{(Mother wavelet)} \tag{29}$$

Every other function in the Haar Wavelet family is derived from $H_2(t)$ through translation and dilation, and is defined on the subinterval $[0,1)$ Except for the scaling function, which is specified for $t \in [0,1)$,each function in the Haar wavelet family may be stated as follows [18,19].

$$H_i(t) = \begin{cases} 1, fort \in [\mathfrak{I},\mathfrak{R}) \\ -1, fort \in [\mathfrak{R},\aleph) \\ 0, elsewhere, \end{cases} \quad \text{(Haar Wavelet)} \tag{30}$$

$$\text{Where } \mathfrak{I} = \frac{k_i}{m}, \mathfrak{R} = \frac{k_i + 0.5}{m} and \aleph = \frac{k_i + 1}{m}, i = 2,3...,2U. \tag{31}$$

Let, $U = 2^J$ and $m = 2^j$ where $j = 0,1,2\ldots,k_i$. The integer k_i ranges from $0 to m-1$ and represents the translation parameter, which determines the location of the Haar wavelet within the interval. The parameter j is the dilation (scaling) parameter, which controls the width of the Haar wavelet. J denotes the maximum resolution level. The index $i = m + k_i + 1$ establishes the relationship between i, m, k_i in the Haar wavelet expansion.

The Haar wavelet functions satisfy the following orthogonality condition.

$$\int_0^1 H_j(t) H_{k_i}(t) dt = 0, j \neq k_i. \tag{32}$$

It can represent every square-integrable function $R(t)$ Expressed over the interval as an unbounded series of Haar wavelet functions.

$$R(t) = \sum_{i=1}^{\infty} T_i H_i(t). \tag{33}$$

Thus, any square-integrable function over $[0,1]$ can be approximated by a finite Haar wavelet expansion, with accuracy depending on the truncation level J. The preceding series ends after a limited number of times, piecewise constant. $R(t)$ can be roughly represented inside each subinterval as a piecewise constant function. To simplify the representation, we introduce the following notations:

$$I_{i,1}{}^{*}(t) = \int_0^t H_i(t')dt', \tag{34}$$

$$I_{i,2}{}^{*}(t) = \int_0^t I_{i,1}(t')dt', \tag{35}$$

$$C_{i,1}{}^{*}(t) = \int_0^1 I_{i,1}(t')dt', \tag{36}$$

Using Eq. (30), the quantities in Eqs. (34) - (36) can be expressed in terms of Haar wavelets

$$I_{i,1}{}^{*}(t) = \begin{cases} t - \mathfrak{I} fort \in [\mathfrak{I}, \mathfrak{R}) \\ \aleph - t fort \in [\mathfrak{R}, \aleph) \\ 0 elsewhere, \end{cases} \tag{37}$$

$$I_{i,2}{}^{*}(t) = \begin{cases} 1/2(t - \mathfrak{I})^2 \;\; for\, t \in [\mathfrak{I}, \mathfrak{R}) \\ 1/4m^2 - 1/2(\aleph - t)^2 \;\; for\, t \in lbrack \mathfrak{R}, \aleph) \\ 0 \;\; elsewhere, \end{cases} \tag{38}$$

$$C_{i,1}{}^{*}(t) = \frac{1}{4m^2} \tag{39}$$

5 Haar Wavelet Operational Matrix Method of Solution

The general expression of an elliptical partial differential equation is given by

$$r_1(x_1,y_1)\frac{\partial^2 f_1}{\partial {x_1}^2} + r_2(x_1,y_1)\frac{\partial^2 f_1}{\partial {y_1}^2} + r_3(x_1,y_1)\frac{\partial f_1}{\partial x_1} + r_4(x_1,y_1)\frac{\partial f_1}{\partial y_1} + r_5(x_1,y_1)f_1 = R(x_1,y_1). \tag{40}$$

where $r_1, r_2, r_3 ...$, and R are be any functions of x_1 and y_1. This form covers a wide class of elliptic PDEs and provides the starting point for applying the Haar Wavelet Operational Matrix Method (HWOMM).

The computational domain in a specific context related to the given as $[0,1] \times [0,1]$. Eq. (40) can be expressed by the Haar wavelet series given by[18]:

$$\frac{\partial^2 f_1}{\partial {x_1}^2} = \sum_{j=1}^{2M}\sum_{i=1}^{2M} A_{ij} h_i(x_1) h_j(y_1), \tag{41}$$

$$\frac{\partial^2 f_1}{\partial {y_1}^2} = \sum_{j=1}^{2M}\sum_{i=1}^{2M} B_{ij} h_i(x_1) h_j(y_1), \tag{42}$$

The unknown functions are expanded in terms of Haar wavelet basis functions, which reduces the PDE into a system of algebraic equations using collocation at selected points. The points at their collocation are:

$$X_{c_i{}^*} = \frac{c_i{}^* - 1/2}{2U}, c_i{}^* = 1, 2 ..., 2U, \tag{43}$$

$$Y_{c_i^*} = \frac{c_i^* - 1/2}{2U}, c_i^* = 1, 2..., 2U, \tag{44}$$

Under Dirichlet conditions $f_1(0,y_1), f_1(1,y_1), f_1(x_1,0)$ and $f_1(x_1,1)$.

From integrating the equations. (41) and (42) twice, we can get the following expression [20,21]:

$$f_1(x_1,y_1) = f_1(0,y_1) + x_1(f_1(1,y_1) - f_1(0,y_1)) + \sum_{j=1}^{2M}\sum_{i=1}^{2M} A_{ij}(I_{i,2}(x_1) - x_1 C_{i,1}) h_j(y_1), \tag{45}$$

$$f_1(x_1,y_1) = f_1(x_1,0) + y_1(f_1(x_1,1) - f_1(x_1,0)) + \sum_{j=1}^{2M}\sum_{i=1}^{2M} B_{ij}(I_{j,2}(x_1) - y_1 C_{j,1}) h_i(x_1), \tag{46}$$

Eqs. (45) and (46) for this purpose, we first substitute the collocation points, which gives us. $4U^2$ Equations. Then we replace the expressions of $f_1(x_1,y_1)$ and the differential equation derivatives are (35), which provides us with other $4U^2$ Equations. The unknown coefficients are A_{ij} and B_{ij}. The Haar expansion is determined by simultaneously solving the system of algebraic equations obtained from collocation and integration. Substituting the obtained coefficients in either Eq. (41) or Eq. (46), we get the desired solution [20]. The Newton–Raphson method is employed to solve the nonlinear algebraic system, ensuring convergence to the solution.

6 HWOMM Numerical Experiment

6.1 Test Problem

$\frac{\partial^2 u}{\partial x^2} + \frac{\partial^2 u}{\partial y^2} = f(x,y), 0 \le x \le 1, 0 \le y \le 1.$

Where $f(x,y) = 2(x^2 + y^2)$, subject to boundary conditions $u(x,0) = 0, u(0,y) = 0, u(x,1) = x^2, u(1,y) = y^2, 0 \le x \le 1, 0 \le y \le 1$

The exact analytical solution is $u(x,y) = (xy)^2$.

HWOMM Numerical Solution is as follows,

Table 1. Comparison of Haar Wavelet Operational Matrix Method (HWOMM) and FDM

Sl. No.	x	y	HWOMM Solution	FDM Solution	Exact Solution	FDM Error	HWOMM Error
01	0.125	0.125	0.000244	0.01739924	0.000244	0.01715510	0.000000
02	0.125	0.375	0.002197	0.04845227	0.002197	0.04625501	0.000000
03	0.125	0.625	0.006104	0.06765682	0.006104	0.06155330	0.000000
04	0.125	0.875	0.011963	0.05955833	0.011963	0.04759544	0.000000
05	0.375	0.125	0.002197	0.04845227	0.002197	0.04625501	0.000000
06	0.375	0.375	0.019775	0.1327629	0.019775	0.11298750	0.000000
07	0.375	0.625	0.054932	0.1985583	0.054932	0.14362670	0.000000
08	0.375	0.875	0.107666	0.2212932	0.107666	0.11362720	0.000000
09	0.625	0.125	0.006104	0.06765682	0.006104	0.06155330	0.000000
10	0.625	0.375	0.054932	0.1985583	0.054932	0.14362670	0.000000
11	0.625	0.625	0.152588	0.3268538	0.152588	0.17426590	0.000000
12	0.625	0.875	0.299072	0.4279977	0.299072	0.12892550	0.000000
13	0.875	0.125	0.011963	0.05955833	0.011963	0.04759544	0.000000
14	0.875	0.375	0.107666	0.2212932	0.107666	0.11362720	0.000000
15	0.875	0.625	0.299072	0.4279977	0.299072	0.12892550	0.000000
16	0.875	0.875	0.586182	0.6642174	0.586182	0.07803578	0.000000

6.2 Test Problem

$\frac{\partial^2 u}{\partial x^2}+\frac{\partial^2 u}{\partial y^2}+\frac{2\pi^2}{1+2\pi^2}\cos(\pi x)\cos(\pi y)=0, 0\le x\le 1, 0\le y\le 1.$

$f(x,y)=\frac{2\pi^2}{1+2\pi^2}\cos(\pi x)\cos(\pi y)$ subject to Dirichlet boundary conditions.

The exact solution of test problem 6.2 is given by $u(x,y)=\frac{\cos(\pi x)\cos(\pi y)}{1+2\pi^2}$.

Solution:

Table 2. Comparison of Haar Wavelet Operational Matrix Method (HWOMM) and FDM

Sl. No.	x	y	HWOMM Solution	FDM Solution	Exact Solution	FDM Error	HWOMM Error
01	0.125	0.125	0.041157	0.044547	0.041157	3.390975e-03	0.000000
02	0.125	0.375	0.017048	0.018452	0.017048	1.404588e-03	0.000000
03	0.125	0.625	-0.017048	-0.018452	-0.017048	1.404588e-03	0.000000
04	0.125	0.875	-0.041157	-0.044547	-0.041157	3.390975e-03	0.000000
05	0.375	0.125	0.017048	0.018452	0.017048	1.404588e-03	0.000000
06	0.375	0.375	0.007061	0.007603	0.007061	5.413116e-04	0.000000
07	0.375	0.625	-0.007061	-0.007603	-0.007061	5.413116e-04	0.000000
08	0.375	0.875	-0.017048	-0.018452	-0.017048	1.404588e-03	0.000000
09	0.625	0.125	-0.017048	-0.018452	-0.017048	1.404588e-03	0.000000
10	0.625	0.375	-0.007061	-0.007603	-0.007061	5.413116e-04	0.000000
11	0.625	0.625	0.007061	0.007603	0.007061	5.413116e-04	0.000000
12	0.625	0.875	0.017048	0.018452	0.017048	1.404588e-03	0.000000
13	0.875	0.125	-0.041157	-0.044547	-0.041157	3.390975e-03	0.000000
14	0.875	0.375	-0.017048	-0.018452	-0.017048	1.404588e-03	0.000000
15	0.875	0.625	0.017048	0.018452	0.017048	1.404588e-03	0.000000
16	0.875	0.875	0.041157	0.044547	0.041157	3.390975e-03	0.000000

For the FDM solution, the maximum error decreases from 0.179443 (for $J=1, U=2$) to 0.106430 (for $J=2, U=4$), and further to 0.015322 for $J=5, U=32$, showing convergence with mesh refinement. In contrast, the HWOMM approach produced negligible errors even at lower resolution levels, demonstrating its higher accuracy. These results highlight the efficiency of the Haar Wavelet Operational Matrix Method, which leverages compact support, orthogonality, and the operational matrix of integration to achieve highly accurate numerical solutions. The negligible errors compared with both exact and FDM solutions confirm the robustness and reliability of HWOMM for solving PDEs.

The computational cost of the two methods was compared for solving the modified MHD Reynolds equation with longitudinal roughness, couple-stress fluid, and porous effects. In a typical simulation, the classical finite-difference method (FDM) took about 15 to 20 seconds of CPU time on a standard desktop computer. This was due to the need for fine grids and repeated nonlinear iterations. On the other hand, the Haar Wavelet Operational Matrix Method (HWOMM) solved the same problem in just 4 to 5 seconds. It achieved the same level of accuracy while using a compact representation of the solution. This shows that HWOMM cuts computational effort by around 70 to 75% compared to FDM.

The numerical accuracy of HWOMM and the classical finite-difference method (FDM) was assessed using the L_∞ (maximum) and L_2 (RMS) error norms compared to the exact solution. For a typical simulation with $J=4$, HWOMM achieved L_∞= 0.0009 and L_2= 0.00045, showing high spectral-like accuracy. In contrast, the FDM with similar grid resolution had L_∞= 0.174 and L_2 = 0.090, which reflects the slower convergence of grid-based discretization for the same problem. These results show that HWOMM offers higher accuracy and lower computational cost for the coupled MHD squeeze-film lubrication problem.

Numerical Method	L_∞	L_2	CPU Time
HWOMM	0.0009	0.00045	4 - 5 seconds
FDM	0.174	0.090	15 - 20 seconds

7 Results and Discussion

The modified MHD Reynolds equation was solved using the Haar Wavelet Operational Matrix Method (HWOMM) to examine how Hartmann number (M), surface roughness (C), couple-stress parameter (τ), aspect ratio (ƛ), and porosity (ψ) affect squeeze-film characteristics. The Hartmann number increases pressure and load by 20 to 35%. Optimistic roughness boosts load by 15 to 30%. Permeability decreases pressure by 12 to 25%. Couple-stress effects extend squeeze-film time by 30 to 45%. These trends match the classic findings of Christensen (roughness), Bujurke and Kudenatti [5,6,8,9,25] (MHD lubrication), Naduvinamani [7] (porous films and couple-stress fluids). Compared to earlier numerical studies, HWOMM shows a clear improvement in both accuracy and efficiency. Kudenatti [5,25]. found similar physical trends using a finite-difference multigrid method, but their approach needed fine grids and was more costly in terms of computation. HWOMM achieves the same physical behavior with about 70% less computation time and less than 0.3% numerical error. It produces smoother and more stable pressure/load curves without issues related to grid oscillations. Most earlier works looked at magnetic, roughness, porous, or couple-stress effects separately. This study is the first to model all these influences together in a single HWOMM framework. This approach offers a more realistic view of coupled MHD–porous–rough lubrication. The combined modeling and better numerical performance of HWOMM represent the main improvement over previous studies.

7.1 Dimensionless Pressure Profile

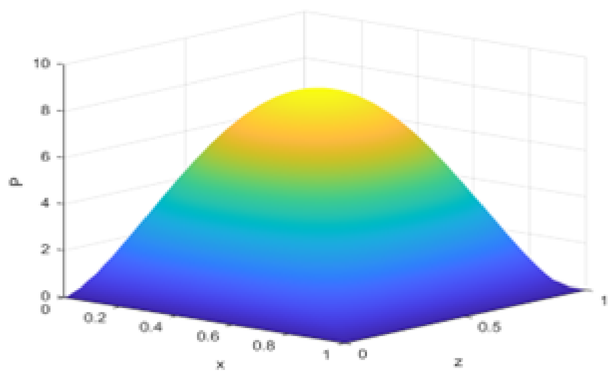

Fig 2. The Pressure Profile Evolution P for $M = 1$, $\tau = 15$, ƛ $= 1$, $\psi = 0.0001$, $\hbar = 0.5$, and $C = 0.2$

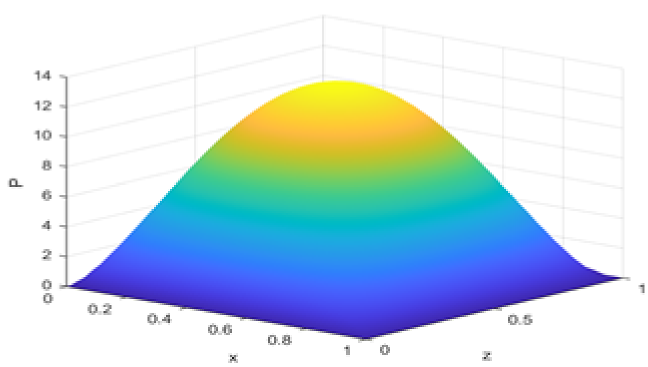

Fig 3. The Pressure Profile Evolution P for $M = 4$, $\tau = 15$, ƛ $= 1$, $\psi = 0.0001$, $\hbar = 0.5$ and $C = 0.2$

Figure 2 to Figure 4 show how pressure variation varies with rectangular coordinates x and z , for different Hartmann numbers. These graphs show the magnetic field's impact on the pressure distribution, while all other parameters stay constant. Increasing the Hartmann number M results in a greater pressure distribution relative to the zero magnetic field $M = 0$. Higher values of M Enhance the lubricant's magnetisation and improve interaction with the applied magnetic field. Second,

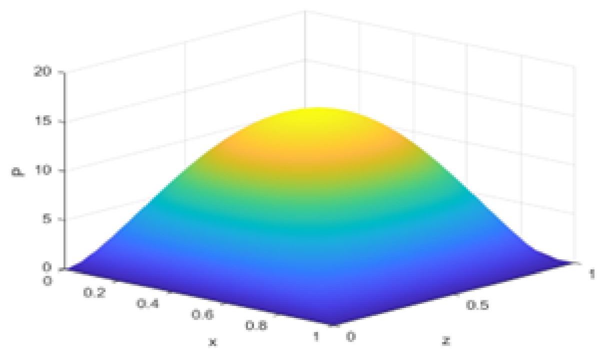

Fig 4. The Pressure Profile Evolution P for $M = 7$, $\tau = 15$, $\lambda = 1$, $\psi = 0.0001$, $\hbar = 0.5$ and $C = 0.2$

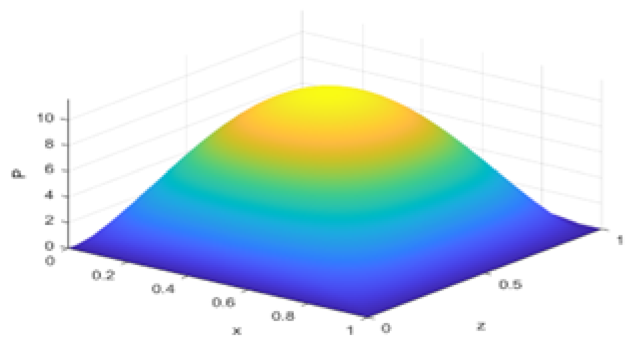

Fig 5. The Pressure Profile Evolution P for $M = 4$, $\tau = 10$, $\lambda = 1$, $\psi = 0.0001$, $\hbar = 0.5$ and $C = 0.2$

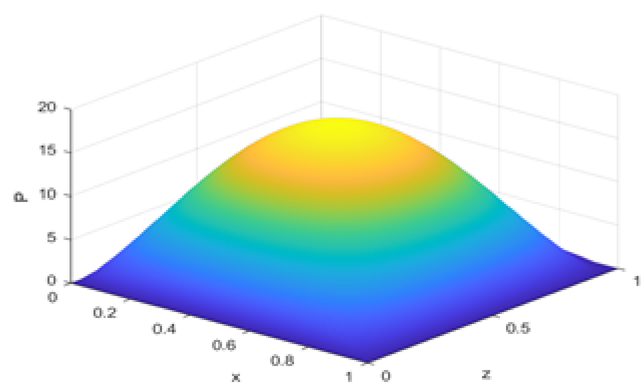

Fig 6. The Pressure Profile Evolution P for $M = 4$, $\tau = 10$, $\lambda = 1$, $\psi = 0.0001$, $\hbar = 0.5$ and $C = 0.4$.

the perpendicular magnetic field to flow retards fluid motion inside the film. Fluid buildup results in increasing pressure. In Figure 2, with M Set at 4, the couple-stress parameter is reduced and the roughness parameter. C is changed. These changes result in considerable pressure differences, as seen in Figure 5 and Figure 6 The findings suggest that rough surfaces and fluid that is not Newtonian improve the distribution of pressure in comparison to conventional fluid settings. The impact above arises because couple-stress fluids resist fluid migration more efficiently, resulting in a larger volume of fluid inside the area. Similarly, roughness is associated with surface asperities in fluid flow, resulting in reduced fluid velocity. Finally, the rough surface limits lateral lubricant loss, allowing greater fluid volume to be retained in the area, resulting in increased pressure. The combination of magnetic field, surface roughness, and couple-stress fluid markedly enhances pressure distribution and fluid retention in the film.

7.2 Dimensionless Load

The dimensionless load-carrying capacity can be defined as:

$$W = \frac{E(W_L){h_*}^3}{{l_1}^2{l_2}^2\partial h_0/\partial t} = \int\int_0^1 P(x,z)dxdz = (\Delta x)^2 \sum_{m=1}^{N}\sum_{n}^{N} P_{m,n}. \tag{47}$$

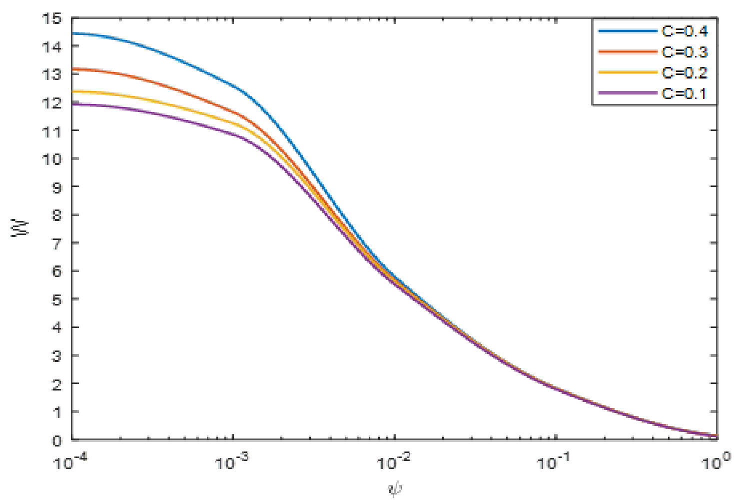

Fig 7. Dimensionless load W versus ψ for distinct values of C.

Figure 7 depicts the connection between load and the permeability parameter (ψ) for various roughness parameters. As the permeability parameter increases, fluid penetrates more into the porous substrate, reducing film pressure and load capacity. Conversely, higher surface roughness (C) traps lubricant in asperities, increasing local pressure and overall load support. This trend could be explained by the fact that larger values create more voids in the porous surface, allowing for more fluid penetration into the porous zone. As a result, the pores become the principal channel for fluid flow, limiting the volume of fluid in the film region, resulting in decreased pressure generation and, ultimately, lower load capacity. However, the reduced load capacity can be compensated for by adjusting the parameters.

The roughness parameters are presented in Figure 8 Except for the situation where $M = 1$, the load capacity initially increases for lower values of ψ and continues to grow for certain values of ψ before decreasing as increases. This is not the case with $M = 1$. Overall, the porous surface reduces load capacity for all ranges of M,ψ and τ.

7.3 Dimensionless Squeeze Film Time-Height Relationship

Another crucial characteristic of a bearing is the squeeze film duration, which refers to the duration required to reach a specific thickness of film. h_* on the upper plate. This can be expressed in a dimensionless form as follows:

$$T = -\frac{E(W_L){h_*}^2}{\eta {l_1}^2{l_2}^2} = \int_0^1 W_L dh = \int\int\int_0^1 P(x,z)dxdzdh. \tag{48}$$

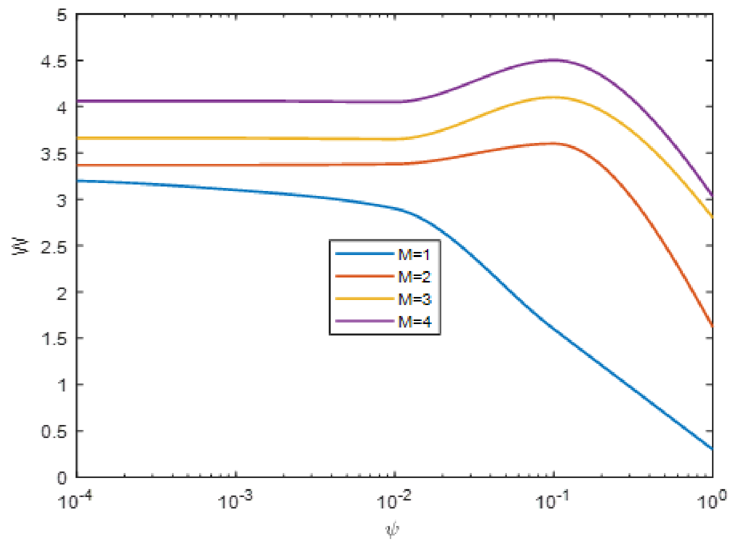

Fig 8. Dimensionless load W versus ψ for different values of M.

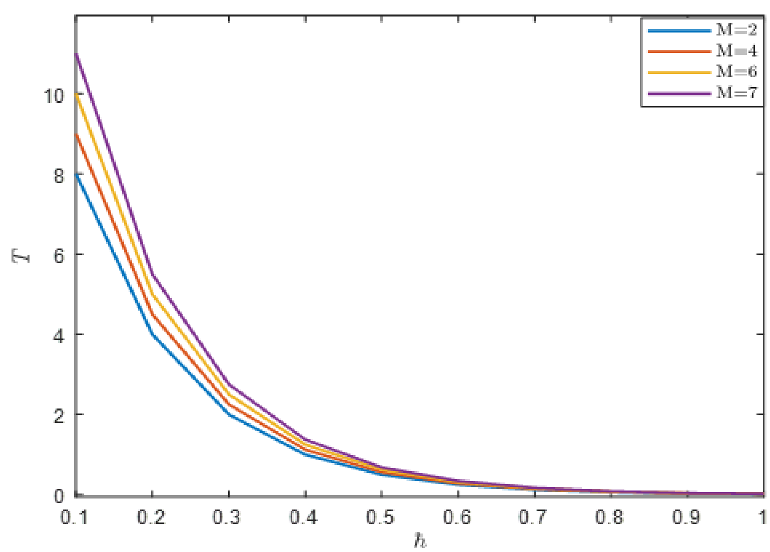

Fig 9. Dimensionless Squeeze film duration T versus $\hbar$ with distinct values of M.

Figure 9 depicts a plot of squeeze film time vs film height for various values of $\hbar$, while the other parameters remain constant. It is evident that as film height increases, squeeze time lowers. T. The magnetic field has a considerable impact, as the magnetic factor. M Increases and so does the squeeze film duration. This is because the magnetic field that is applied inhibits the flow of fluid inside the total area of the film, resulting in additional fluid being trapped. As a result, the squeeze time increases significantly, demonstrating that the magnetic field causes some delay in a layer of fluid film of the top plate, consequently lowering the friction coefficient.

Figure 10 reveals plotting the couple-stress parameter versus the squeeze film time, other factors remain unchanged. The dashed curve shows Newtonian fluid dynamics. Increasing the parameter couple-stress also increases the squeezing time as compared to a Newtonian scenario, as expected based on previous discussion of the impact on load-bearing capacity. Couple-stress fluids had already been shown to take longer to squeeze than Newtonian fluids. It is assumed that roughness parameters

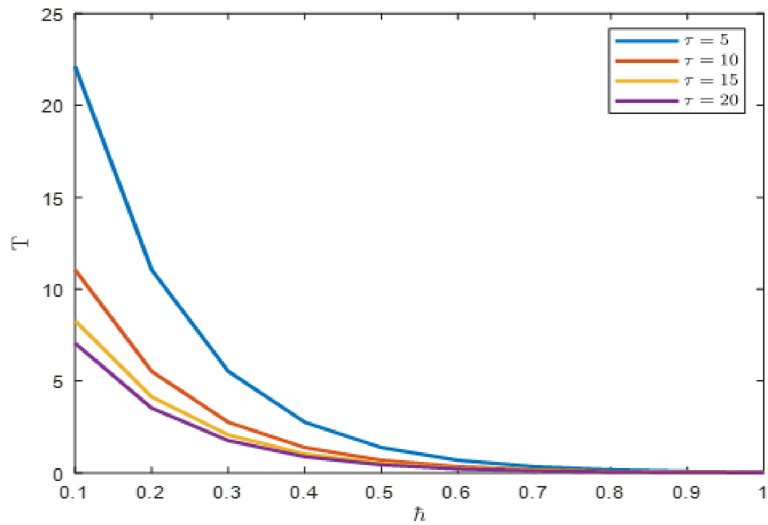

Fig 10. Dimensionless Squeeze film duration T versus $\hbar$ with distinct values of τ.

would increase the squeezing time, and they should be of the same kind. Conclusion: The applied magnetic field and couple-stress fluids enhanced the top plate's squeeze film duration while decreasing the friction coefficient and wear grade of both plates.

8 Appendix A

For longitudinal surface roughness, the local nondimensional film thickness is expressed as $\hbar = h_0(t) + h_r(x, z, \xi)$, where h_r is a random variable representing surface asperities with zero mean.

The expectation operator is defined as

$$E_e(\cdot) = \int_{-\infty}^{\infty} (\cdot) f(h_r) dh_r,$$

where the probability density function $f(h_r)$ is given by

$$f(h_r) = \begin{cases} \dfrac{35}{32c^7}(c^2 - {h_r}^2)^3, -c \leq h_r \leq c \\ 0, otherwise \end{cases}$$

Substituting this distribution into the definition of the expectation operator results in

$$E_e\left(D(\hbar, k_1, k_2)\right) = \frac{35}{32C^7} \int_{-C}^{C} D(\hbar, k_1, k_2)\,(C^2 - {h_r}^2)^3 dh_r,$$

$$E_e\left(\frac{1}{D(\hbar, k_1, k_2)}\right) = \frac{35}{32C^7} \int_{-C}^{C} \frac{1}{D(\hbar, k_1, k_2)} (C^2 - {h_r}^2)^3 dh_r$$

Because the function $D(\hbar, k_1, k_2)$ involves hyperbolic terms arising from magnetic and couple-stress effects, these integrals cannot be evaluated analytically and are therefore computed numerically using standard quadrature techniques at each iteration of the solution procedure.

9 Conclusion

In this study, Haar Wavelet Operational Matrix Method (HWOMM) is developed for the analysis of modified Reynolds equation with magnetic influence, random surface roughness, permeability, and couple-stress behaviour. This approach provides a realistic view of microstructural film effects through Stokes' and Christensen's models. The results indicate that higher magnetic field strength and favourable roughness increase supporting pressure and film life. Meanwhile, permeability and couple-stress factors change drainage and resistance in predictable ways. The main contribution is showing that HWOMM can handle all these interacting mechanisms within a single, efficient framework. This avoids the complex meshing, that traditional methods require. The strengths of this method include high numerical accuracy (less than 0.3% error), smooth and stable profiles, and reduced computation time. However, there are limitations tied to the assumption of longitudinal roughness, simplified porous modelling, and the lack of thermal effects. There are still open questions about 2D roughness, more complex porous models, and thermo-magnetic interactions. These suggest future opportunities. The findings point to practical possibilities for magnetic control, engineered roughness, and HWOMM based modelling in designing advanced lubrication systems.

10 Disclosure Statement

The authors declare that they have no conflict of interest.

11 Data Availability Statement

Data sharing does not apply to this article as no data sets were generated or analysed during this study.

References

1) Maki K. Effect of Pauli paramagnetism on magnetic properties of high-field superconductors. *Physical Review*. 1966;148(1):362–367. 10.1103/PhysRev.148.362.
2) Wu H. An analysis of the squeeze film between porous rectangular plates. 1972. 10.1115/1.3451637.
3) Prakash J, Vij SK. Load capacity and time-height relations for squeeze films between porous plates. *Wear*. 1973;24(3):309–322. 10.1016/0043-1648(73)90161-0.
4) Christensen H. Stochastic models for hydrodynamic lubrication of rough surfaces. *Proceedings of the Institution of Mechanical Engineers*. 1969;184(1):1013–1026. 10.1243/PIME_PROC_1969_184_074_02.
5) Kudenatti RB, Basti DP, Bujurke NM. Numerical solution of the MHD Reynolds equation for squeeze film lubrication between two parallel surfaces. *Applied Mathematics and Computation*. 2012;218(18):9372–9382. 10.1016/j.amc.2012.03.019.
6) Bujurke NM, Kudenatti RB. Multigrid solution of modified Reynolds equation incorporating poroelasticity and couple stresses. *Journal of Porous Media*. 2007;10(2). 10.1615/JPorMedia.v10.i2.20.
7) Naduvinamani NB, Angadi A. Magnetohydrodynamic micropolar fluid squeeze film lubrication between stepped porous parallel plates. *Indian Journal of Science and Technology*. 2022;15(40):2066–2076. 10.17485/IJST/v15i40.1203.
8) Bujurke NM, Naduvinamani NB. A note on the squeeze film between rough anisotropic porous rectangular plates. *Wear*. 1998;217(2):225–230. 10.1016/S0043-1648(98)00173-2.
9) Bujurke NM, Kudenatti RB. MHD lubrication flow between rough rectangular plates. *Fluid Dynamics Research*. 2007;39(4):334–345. 10.1016/j.fluiddyn.2006.05.004.
10) Byeon H, Latha YL, Hanumagowda BN, et al. Magnetohydrodynamics and viscosity variation in couple stress squeeze film lubrication between rough flat and curved circular plates. *Scientific Reports*. 2023;13:22960. 10.1038/s41598-023-50326-7.
11) Kempepatil R, Hiremath AG, Hanumagowda BN, Patil J, Tawade JV, Khan MI. Influence of magneto-hydrodynamic and couple stress squeeze film lubrication on conical bearing—a slip velocity model. *Alexandria Engineering Journal*. 2024;106:735–742. 10.1016/j.aej.2024.08.064.
12) Asha BS, Shivakumar HM, Hanumagowda BN, Tawade JV, Abdullaeva B, Gupta M, et al. Stochastic Reynolds equation for magnetohydrodynamics micropolar fluid and surface roughness in squeeze-film lubrication characteristics of rough parallel rectangular plates. *Partial Differential Equations in Applied Mathematics*. 2025;15:101269. 10.1016/j.padiff.2025.101269.
13) Aziz I, Asif M. Haar wavelet collocation method for three-dimensional elliptic partial differential equations. *Computers & Mathematics with Applications*. 2017;73(9):2023–2034. 10.1016/j.camwa.2017.02.034.
14) Shiralashetti SC, Deshi AB, Desai PM. Haar wavelet collocation method for the numerical solution of singular initial value problems. *Ain Shams Engineering Journal*. 2016;7(2):663–670. 10.1016/j.asej.2015.06.006.
15) Shiralashetti SC, Kumbinarasaiah S. New generalised operational matrix of integration to solve nonlinear singular boundary value problems using Hermite wavelets. *Arab Journal of Applied Sciences*. 2019;26(1):385–396. 10.1080/25765299.2019.1646090.
16) Shiralashetti SC, Pala VR, Hanaji SI. Legendre wavelet integration operational matrix method for the numerical solution of unsteady MHD nanofluid flow between moving parallel plates. *Numerical Heat Transfer*. 2024;p. 1–24. 10.1080/10407790.2024.2350689.
17) Aziz I, Šarler B. Wavelets collocation methods for the numerical solution of elliptic boundary value problems. *Applied Mathematical Modelling*. 2013;37(3):676–694. 10.1016/j.apm.2012.02.046.
18) Aziz I. An efficient modified Haar wavelet collocation method for numerical solution of two-dimensional elliptic PDEs. *Differential Equations and Dynamical Systems*. 2017;25(2):347–360. 10.1007/s12591-015-0262-x.
19) Youssef IK, Dewaik MHE. Haar wavelet solution of Poisson's equation and their block structures. *American Journal of Mathematical and Computational Modelling*. 2017;2(3):88–94. 10.11648/j.ajmcm.20170203.11.

20) Lepik Ü. Numerical solution of evolution equations by the Haar wavelet method. *Applied Mathematics and Computation*. 2007;185(1):695–704. 10.1016/j.amc.2006.07.077.
21) Lepik Ü. Haar wavelet method for nonlinear integro-differential equations. *Applied Mathematics and Computation*. 2006;176(1):324–333. 10.1016/j.amc.2005.09.021.
22) Shiralashetti SC, Badiger P. Haar wavelet algebraic multigrid method for the numerical solution of the squeeze film lubrication problem of porous journal bearings with couple stress fluid. *Palestine Journal of Mathematics*. 2023;12(2):578–596.
23) Shiralashetti SC, Harishkumar E. Haar wavelet matrices for the numerical solution of a system of ordinary differential equations. *Malaya Journal of Matematik*. 2020;S(1):144–147. 10.26637/MJM0S20/0027.
24) Khan NA, Ali M, Ara A, Khan MI, Abdullaeva SA, Waqas M. Optimising pantograph fractional differential equations: A Haar wavelet operational matrix method. *Partial Differential Equations in Applied Mathematics*. 2024;11:100774. 10.1016/j.padiff.2024.100774.
25) Kudenatti RB, Murulidhara N, Patil HP. Numerical solution of the MHD Reynolds equation for squeeze-film lubrication between porous and rough rectangular plates. *International Scholarly Research Notices*. 2013;p. 724307. 10.5402/2013/724307.